



A nonlinear hybrid energy harvester with high ultralow-frequency energy harvesting performance

Kai Wang · Huajiang Ouyang · Jiayi Zhou · Yaopeng Chang · Daolin Xu · Huai Zhao

Received: 27 September 2020 / Accepted: 3 December 2020 / Published online: 25 January 2021
© Springer Nature B.V. 2021

Abstract The exploration of renewable energy technology is increasingly important owing to depletion of fossil fuels and the environmental pollution caused by the use of fossil fuels. Converting mechanical energy to electrical energy is one approach to developing renewable energy. However, the harvesting of ultralow-frequency mechanical energy is a challenge that limits the development of energy harvesting technology. To address this difficult problem, this paper proposes a nonlinear hybrid energy harvester in which an electromagnetic generator (EMG) and a triboelectric generator (TEG) are coupled to harvest the mechanical energy from ambient vibrations at ultralow frequencies. The energy harvester is combined with a quasi-zero-stiffness (QZS) mechanism composed of four QZS springs and a linear spring to produce a large-amplitude response and improve the energy harvesting performance. The effect of the mechanical condition (linear,

quasi-zero-stiffness and bistable) on the efficiency of energy harvesting is analysed analytically and verified by theoretical and numerical analyses. The dynamics responses of the nonlinear energy harvester influenced by systematic parameters are also dissected. This work provides a guideline for improving the ultralow frequency ambient vibration energy harvesting performance of a TEG through nonlinearity.

Keywords Nonlinearity · Ultralow-frequency mechanical energy · Quasi-zero-stiffness · Electromagnetic generator · Triboelectric generator

1 Introduction

Petroleum and coal are two major sources of energy supply for modern society. However, both of them are non-renewable energy resources and produce greenhouse gases, which will seriously constrain the development of both economy and society. Therefore, the exploration of renewable energy, including solar energy, tidal energy, nuclear power, wind power and wave energy, have aroused widespread interest among researchers [1–3]. Furthermore, harvesting energy from ambient vibration is another avenue to produce renewable energy supplies for wireless sensors and other equipment that do not allow easy replacement of batteries. Various energy harvesting ideas have attracted much attention [4].

K. Wang · J. Zhou (✉) · Y. Chang · D. Xu
College of Mechanical and Vehicle Engineering, Hunan University, Changsha 410082, People's Republic of China
e-mail: jxizhou@hnu.edu.cn

H. Ouyang · H. Zhao
School of Engineering, University of Liverpool,
Liverpool L69 3GH, UK

D. Xu
State Key Laboratory of Advanced Design and
Manufacturing for Vehicle Body, Hunan University,
Changsha 410082, People's Republic of China

Up till now, the mechanisms to convert mechanical energy to electrical energy mainly include electromagnetic [5], magnetoelectric [6], electrostatic [7], piezoelectric [8] and pyroelectric [9]. Energy harvesting performance is highly related to the types of the excitation source and the operating mechanism applied to harvest energy [10]. Generally, piezoelectric energy harvesters and electrostatic energy harvesters have better energy harvesting performance under high-frequency excitations, while electromagnetic energy harvesters and magnetoelectric energy harvesters can effectively convert low-frequency vibratory energy to electrical energy [11].

All of these energy harvesters with different physical principles can be utilized to harvest energy from ambient vibration. Fan et al. [12] put forward a monostable electromagnetic energy harvester to realize efficient energy harvesting from low-frequency vibration. Halim et al. [6, 13] converted from human-limb motion by an electromagnetic energy harvester that can up-convert the low-frequency vibration to a high-frequency one. Zhu et al. [14] investigated an electromagnetic inertial mass damper energy harvester for mitigating the vibration and harvesting energy simultaneously. Yang et al. [15] put forward a multi-frequency electromagnetic energy harvester. Foong et al. [16] proposed an anti-phase electromagnetic energy harvester to increase the output power. Liu et al. [17] minimized the overall volume of the electromagnetic energy harvester by a dual Halbach arrays. Zhang et al. [18] designed a rolling magnet electromagnetic energy harvester and improved the energy harvesting performance by introducing a friction effect. Castagnetti [5, 19, 20] engineered energy harvesters based on fractal geometry, a pendulum structure and Belleville springs to improve the low-frequency vibration energy harvesting performance.

As a typical application of the electrostatic mechanism, a triboelectric generator (TEG) has attracted increasing attention since it was proposed by Wang et al. [21]. Wang et al. [22] presented a sliding-triboelectric generator based on the relative sliding between two contacting planes. He et al. [23] demonstrated a square-grid TEG to convert the vibration energy to electrical energy over a broad bandwidth. Bhatia et al. [24] also reported a TEG that could harvest vibration energy in a wide frequency range. To harvest energy from low-frequency vibration better,

Wu et al. [25] proposed a single-spring resonator based on the TEG. Fu et al. [26] investigated the effect of electrical properties on the dynamic features of a TEG.

To convert mechanical energy to electrical energy efficiently, designing an energy harvester making use of more than one electric transduction principle is a promising approach [27]. In some previous publications, several kinds of hybrid energy harvesters were devised by combining an electromagnetic generator (EMG) and a TEG [28]. Other mechanisms of electricity generation mentioned above can be combined together to construct different types of hybrid energy harvesters [29].

Generally, an energy harvester has an optimal harvesting performance at the resonant frequency of a system (except the contact-mode triboelectric energy harvester [30]), owing to the large-amplitude response at such a frequency. Therefore, it is important to design an energy harvester system with low resonant frequency to harvest low-frequency vibration energy. Unfortunately, it is difficult to design an energy harvester using linear stiffness and lightweight mass to achieve ultralow resonant frequency, and thus a linear energy harvester always fails to produce a large-amplitude resonance at ultralow frequencies [31]. Fortunately, the quasi-zero-stiffness (QZS) mechanism could provide a configuration with an ultralow and even zero stiffness feature, which enables an energy harvester to achieve ultralow resonant frequency. In some previous works, the QZS mechanism has been utilized to design vibration isolators for isolating ultralow frequency vibrations [32–34] and metamaterials for manipulating ultralow frequency waves [35–37]. Nevertheless, for a conventional QZS (CQZS) system, the near-zero stiffness only occurs in a small displacement range around the static equilibria, and increases obviously with the increase of the displacement. This might prevent a harvester from producing large-amplitude resonance.

In order to harvest the vibration energy in the ultralow frequency region effectively, a dual QZS (DQZS) system is put forward by replacing the inclined spring with a QZS spring (a paired magnet ring connecting a linear spring in parallel). By removing the QZS spring or adjusting the compression of the horizontal coil spring in the QZS spring, the system could produce different mechanical mechanisms: a linear mechanism, a CQZS mechanism, a

DQZS mechanism and a bistable mechanism. Based on such a mechanical configuration and coupling an electromagnetic generator (EMG) and a triboelectric generator (TEG), this paper presents a new nonlinear hybrid energy harvester. The energy harvesting performance for each mechanical mechanism is evaluated analytically and verified numerically. The nonlinear dynamic characteristics and the effects of systematic parameters on the energy harvesting performance are also studied.

2 Structural details

2.1 Model and principle

A schematic diagram of the hybrid energy harvester is shown in Fig. 1. The configuration includes two components: the mechanical structure and the energy harvester system. The mechanical structure was obtained by upgrading a CQZS system by replacing the inclined linear spring with a QZS spring. The QZS spring consists of a set of paired magnet rings and a linear spiral spring, and is used to provide negative stiffness along the vertical direction. To ensure that the guide rod in the QZS spring moves only in the axial direction, two sliding bearings are installed in the spring, which are also used to decrease the damping by changing the sliding friction to rolling one. One end of the QZS spring is hinged on the platform, and the other is hinged on the frame of the main structure. In the initial configuration of the energy harvester, which is also the static equilibrium configuration, the QZS spring is perpendicular to the platform; the spiral

springs in the QZS springs are compressed, and the platform is supported by the linear spring alone. When an excitation is applied to the energy harvester, the force balance is broken, and the platform deviates from the equilibrium configuration, causing the energy harvester to harvest energy from ambient vibration.

To avoid collisions between the platform and the bottom of the energy harvester, a limiting stopper is installed at the bottom. The energy harvester system has two components, a triboelectric generator (TEG) and an electromagnetic generator (EMG) that is comprised of a Halbach array [38] and a coil. The presented energy harvester possesses a cylindrical appearance with a diameter of $2b + w$ and a height of about three times of w . Variables b and w denote the length of the QZS spring at the rest equilibrium position and the width of the dielectrics in the TEG, respectively. The operating principle of the energy harvester is presented in Fig. 2, and the electrical parameters are listed in Table 1. Note that some of the parameters are selected from previous studies [39, 40]. Figure 2a shows the operating principle of the TEG, and Fig. 2b shows a schematic diagram of the QZS spring in different states. Figure 2c illustrates the operating principle of the EMG.

Initially, as shown in Fig. 2b-I, the energy harvester is in the static equilibrium configuration. Dielectric 1 and Dielectric 2 in the TEG overlap completely and are in close contact with each other. Because of the very large difference in their electron-attracting abilities, electrons are transferred from Dielectric 2 to Dielectric 1, and their surfaces become positively and negatively charged, respectively. Because the separation between the surfaces of Dielectric 1 and Dielectric

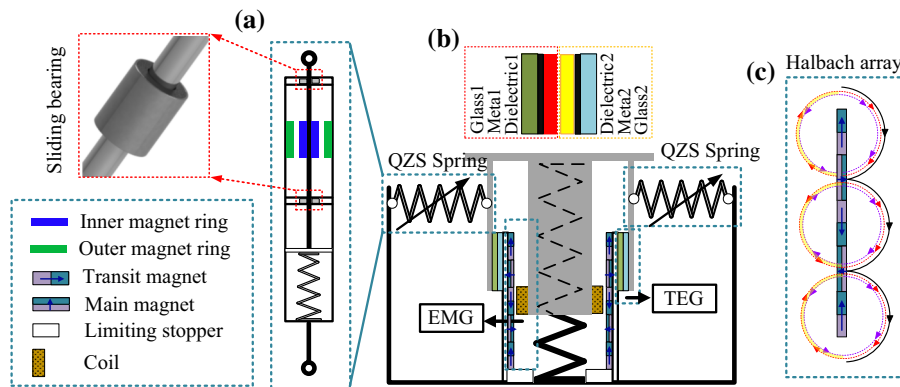


Fig. 1 Schematic diagram of **a** QZS spring, **b** the hybrid energy harvester and **c** the Halbach array

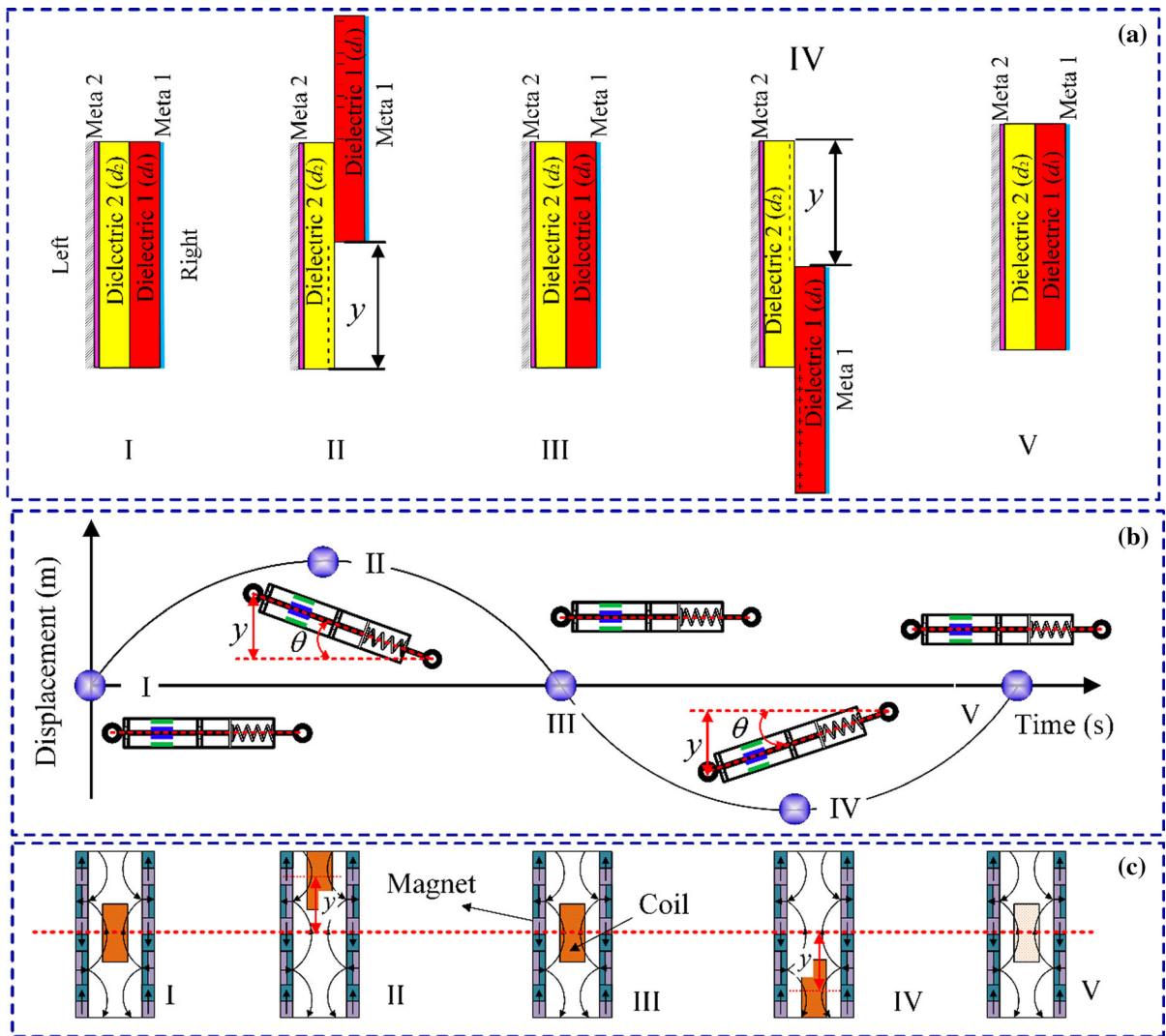


Fig. 2 Operating principle of the EMG and TEG within one cycle of motion. **a** Operating principle of the TEG, **b** schematic diagram of the negative stiffness mechanism at different times,

and **c** operating principle of the EMG. The terms of ‘Meta 1’ and ‘Meta 2’ denote metal electrodes deposited on right-hand dielectric and left-hand dielectric, respectively

2 is negligible in the contact area, and the charges on the surface will not escape quickly, there will be a small difference in electric potential across the two electrodes. Under excitation, the mechanical structure of the energy harvester will deviate from the static equilibrium configuration (Fig. 2b-II). Because Dielectric 2 is fixed on the platform and Dielectric 1 is fixed on the base, the relative motion of the base and platform causes Dielectric 2 to move away from Dielectric 1, causing the charge distribution to become unstable (Fig. 2a-II). Then, an electric field is generated and drives a current flow from the left-hand

electrode to the right-hand electrode, which cancels the tribo-charge-induced potential. When the energy harvester reaches its peak displacement, Dielectric 1 and Dielectric 2 are separated by the largest distance (no more than $0.9 l$ [40]) (Fig. 2-II). Then Dielectric 1 moves downward and returns to its static equilibrium position (Fig. 2-III) [22].

As Dielectric 1 continues to move downward, the two dielectrics move away from each other in the opposite direction compared with Fig. 2a-II. Note that the operating principle of triboelectrification is the same as that when Dielectric 1 moves upward.

Table 1 Utilized parameters in the calculation of hybrid energy harvester’s static characteristics

Parameter	Value
Magnetic pole surface density	$\sigma_{\text{MPSD}} = 1 \text{ T}$
Permeability of vacuum	$\mu_0 = 4\pi \times 10^{-7} \text{ N/A}$
Inner radius of the inner permanent magnet	$r_{\text{inner}} = 2 \text{ mm}$
Width of inner and outer permanent magnets	$l = 4 \text{ mm}$
Height of inner and outer permanent magnets	$h = 5 \text{ mm}$
Air gap between the inner and outer permanent magnets	$g = 2 \text{ mm}$
Length of the QZS spring at the rest equilibrium position	$b = 80 \text{ mm}$
Stiffness of the vertical spring	$K = 2 \times 10^4 \text{ N/m}$
Stiffness of the magnet ring in the equilibrium position	$k^* = 6.42 \times 10^3 \text{ N/m}$
Mass of the platform	$M = 5 \text{ kg}$

Therefore, the motion of Dielectric 1 from its static equilibrium position to its maximum negative position is not described.

When an excitation is applied to the energy harvester, the permanent magnet block of the EMG leaves its static equilibrium position and moves relatively to the coil fixed on the frame of the energy harvester. The change in magnetic flux within the coil induces an electric potential in the coil owing to electromagnetic induction. If an electrical load is connected to the circuit, a current can be produced [41].

2.2 Static analysis

First, a static analysis of the hybrid energy harvester is conducted. Under excitation, the mechanical structure of the energy harvester deviates from its static equilibrium position by a distance y , and the QZS spring rotates around the hinge point by an angle θ (Fig. 2b). In addition, the permanent magnetic rings in the negative stiffness mechanism also deviate from their static equilibrium position by a distance x . According to Ref. [42], the restoring force of the QZS spring can be given by

$$f_{\text{NSM}}^* = k_H x - f_{\text{PMR}}(x) \tag{1}$$

where $f_{\text{PMR}}(x) = \frac{\sigma_{\text{MPSD}}^2 R_m}{\mu_0} [2\phi(x) - \phi(x+h) - \phi(x-h)]$ denotes the thrust force of the magnet ring, and $\sigma_{\text{MPSD}} = \mathbf{J} \cdot \mathbf{n}$ denotes the magnetic pole surface density. \mathbf{J} is the magnetic polarisation vector, \mathbf{n} is the unit normal vector, and μ_0 is the permeability of vacuum. $R_m = g/2 + r_{\text{inner}} + l$ is the average radius of the inner and

outer permanent magnets, where r_{inner} , l , and g denote the inner radius of the inner permanent magnet, the width of both the inner and outer permanent magnets, and the air gap between the inner and outer permanent magnets, respectively. In addition, h denotes the height of both the inner and outer permanent magnets, and

$$\begin{aligned} \phi(a) = & (2l + g) \arctan\left(\frac{2l + g}{a}\right) - 2(l + g) \\ & \arctan\left(\frac{l + g}{a}\right) + g \arctan\left(\frac{g}{a}\right) \\ & - \frac{a}{2} \left\{ \ln\left[(2l + g)^2 + a^2\right] \right. \\ & \left. - 2 \ln(l + g)^2 + \ln(g^2 + a^2) \right\} \end{aligned} \tag{2}$$

where a denotes a variable. By differentiating the expression for the restoring force Eq. (1) with respect to the displacement x , and substituting $x = 0$ into the derived stiffness expression, one can obtain the stiffness provided by the magnet ring in the QZS spring as

$$k^* = \frac{\sigma_{\text{MPSD}}^2 R_m}{\mu_0} \left\{ \frac{4h^2}{h^2 + (l + g)^2} + \ln \frac{[(2l + g)^2 + h^2](g^2 + h^2)}{(2l + g)^2 g^2} \right\} \tag{3}$$

By substituting Eq. (3) into Eq. (1), the QZS restoring force can be written as

$$\begin{aligned} f_{\text{NSM}} = & k^* x \\ & - \frac{\sigma_{\text{MPSD}}^2 R_m}{\mu_0} [2\phi(x) - \phi(x+h) - \phi(x-h)] \end{aligned} \tag{4}$$

In this study, the QZS spring provides negative stiffness in the energy harvester. Therefore, both the permanent magnet ring and the horizontal spring apply a thrust force to the energy harvester. In addition, to evaluate the effect of the horizontal spring in the QZS mechanism on the mechanical features of the energy harvester, a parameter γ is introduced into the expressions for the restoring force and stiffness. Note that γ , which is referred to as the stiffness ratio, represents the ratio of the stiffness of the negative stiffness mechanism in the static equilibrium configuration to that of the horizontal spring. At this point, the thrust force provided by the QZS spring to the energy harvester is given by

$$f_{NSM,TH} = \gamma k^* (\delta - x) + \frac{\sigma_{MPSD}^2 R_m}{\mu_0} [2\phi(x) - \phi(x+h) - \phi(x-h)] \tag{5}$$

where δ is the compression of the horizontal spring in the QZS mechanism in the static equilibrium configuration. According to the geometry of the mechanical configuration, the restoring force of the energy harvester can be expressed as

$$F(y) = Ky - 4f_{NSM,TH}(x) \sin(\theta) \tag{6}$$

where K denotes the stiffness of the vertical spring, and the sine function is expanded as $\sin(\theta) = y/\sqrt{b^2 + y^2}$, where b is the length of the QZS spring in the static equilibrium configuration. Furthermore, the displacement x of the inner permanent magnet ring can be expressed as the vertical displacement, namely, $x = \sqrt{b^2 + y^2} - b$. Therefore, the stiffness of the energy harvester can be obtained by substituting the sine function into the restoring force and differentiating the result with respect to the vertical displacement y

$$K_{EH} = K - 4\gamma k^* \left[\frac{b^2 (\delta - \sqrt{b^2 + y^2} + b)}{(b^2 + y^2)^{\frac{3}{2}}} - \frac{y^2}{b^2 + y^2} \right] - p_1 - p_2 \tag{7}$$

where

$$\begin{cases} p_1 = \frac{4\sigma_{MPSD}^2 R_m b^2 [2\phi(\sqrt{b^2 + y^2} - b) - \phi(\sqrt{b^2 + y^2} - b + h) - \phi(\sqrt{b^2 + y^2} - b - h)]}{\mu_0 (y^2 + b^2)^{\frac{3}{2}}} \\ p_2 = \frac{4y^2 \sigma_{MPSD}^2 R_m [2\phi(\sqrt{b^2 + y^2} - b) - \phi(\sqrt{b^2 + y^2} - b + h) - \phi(\sqrt{b^2 + y^2} - b - h)]}{\mu_0 (y^2 + b^2)} \end{cases} \tag{8}$$

Note that the function $\phi(a)$ in the expression can be expanded as [43]

$$\phi(a) = -\frac{2a^2}{a^2 + (l + g)^2} - \frac{1}{2} \ln \frac{[(2l + g)^2 + a^2](g^2 + a^2)}{(l + g)^4} \tag{9}$$

By deriving the QZS condition $\gamma k^*/K = b/4\delta$ and substituting it into Eqs. (6) and (7), the expressions for the restoring force and stiffness of the energy harvester with the QZS mechanism can be written as

$$F_{HEH,QZS} = K \left[y - \frac{by(\delta - x)}{\delta \sqrt{y^2 + b^2}} \right] - \frac{4\sigma_{MPSD}^2 R_m y}{\mu_0 \sqrt{y^2 + b^2}} [2\phi(x) - \phi(x+h) - \phi(x-h)] \tag{10}$$

$$K_{HEH,QZS} = K \left\{ 1 - \frac{b}{\delta} \left[\frac{b^2 (\delta - \sqrt{b^2 + y^2} + b)}{(b^2 + y^2)^{\frac{3}{2}}} + \frac{y^2}{b^2 + y^2} \right] \right\} - p_1 - p_2 \tag{11}$$

2.3 Static characteristics

For the structural parameters in Table 1, the stiffness of the hybrid energy harvester for different γ is shown in Fig. 3. Figure 3a shows a contour plot, and Fig. 3b shows the relationship between the stiffness and the displacement for stiffness ratios of $\gamma = 0.5$, $\gamma = 0.77$, and $\gamma = 0.9$. The black and white solid lines in Fig. 3a represent stiffness values of 1000 and 0 N/m, respectively. The grey area represents the parameter region in which the stiffness is zero. Clearly, the stiffness can be changed by varying γ .

More importantly, a threshold value of γ appears at the intersection of the two white lines in Fig. 3a. As shown in Fig. 3b, when γ is 0.77, the energy harvester

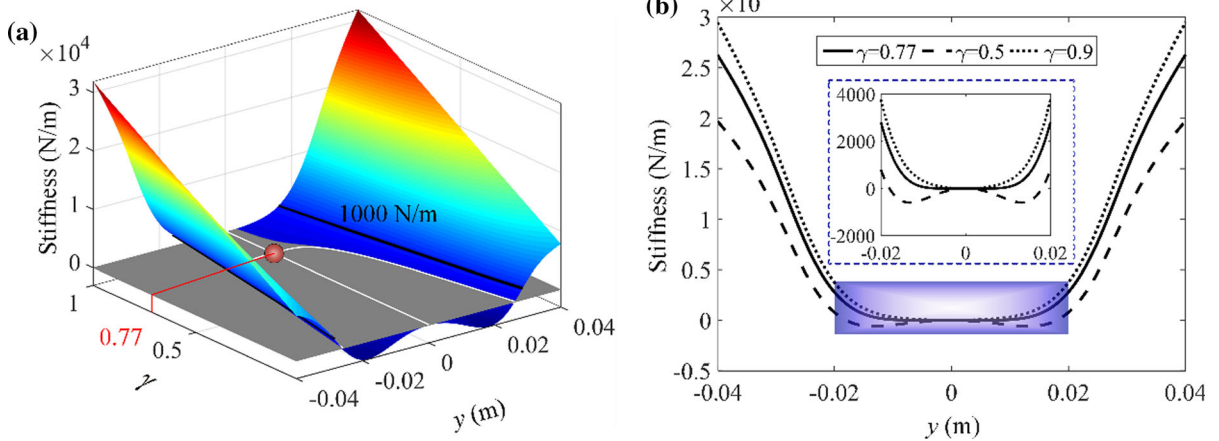


Fig. 3 Stiffness of the energy harvester for different γ . **a** surface plot of stiffness and **b** stiffness versus displacement for stiffness ratios γ of 0.5, 0.77, and 0.9. The grey area in (a) indicates the parameter region in which the stiffness is equal to 0 N/m

has the largest displacement region, in which the stiffness is very low. Such an appealing stiffness feature is beneficial to decrease the resonant frequency of the energy harvester and amplify its dynamical responses. When γ exceeds the threshold, the stiffness of the energy harvester clearly increases, and the low-stiffness region becomes smaller. By contrast, when γ is below the threshold value of 0.77, the stiffness of the energy harvester becomes negative near the equilibrium configuration. Thus, the structure is bistable.

To further analyse the effect of γ on the energy harvester, the potential energy is analysed. The potential energy of the restoring force $F_{HEH,QZS}$ can be expressed as

$$\begin{aligned}
 U_P(y) &= \int_0^y F_{HEH,QZS}(\varepsilon) d\varepsilon \\
 &= \frac{1}{2}Ky^2 + \frac{b}{\delta} \left[\frac{1}{2}y^2 - (\delta + b)\sqrt{b^2 + y^2} \right] \\
 &\quad + \frac{b^2}{\delta}(\delta + b) - \frac{4\sigma_1^2 R_m}{\mu_0} \left(\int_0^y \frac{2y\phi(x)}{\sqrt{y^2 + b^2}} dy \right. \\
 &\quad \left. - \int_0^y \frac{y\phi(x+h)}{\sqrt{y^2 + b^2}} dy - \int_0^y \frac{y\phi(x-h)}{\sqrt{y^2 + b^2}} dy \right) \tag{12}
 \end{aligned}$$

where ε denotes a variable of integration.

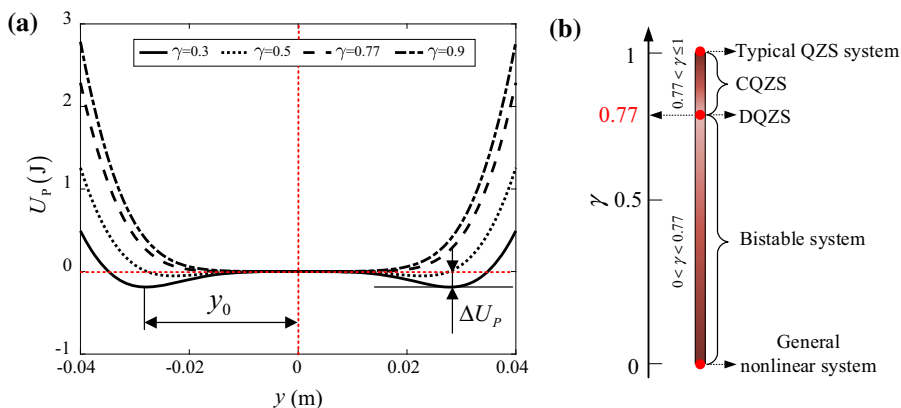
Figure 4a, b show the potential energy curves and mechanical properties, respectively, of the energy harvester at different stiffness ratios. The dashed-

dotted and dashed lines in Fig. 4a denote the potential energy profiles for $\gamma = 0.77$ and $\gamma = 0.9$, respectively. In both cases, the energy harvester is monostable; that is, there is only one equilibrium. By contrast, when $\gamma = 0.5$ and $\gamma = 0.3$ (dotted and solid lines, respectively), the energy harvester switches to a bistable state.

The potential energy is locally maximised in the unstable central configuration, whereas the adjacent stable equilibria at $y = \pm y_0$ locally minimise the potential energy of the energy harvester. Specifically, the bistable mechanism has a double-well restoring-force potential with two stable equilibria and one unstable equilibrium. According to the principle of minimum total potential energy, disturbances to the energy harvester when it is initially placed at the unstable equilibrium will push the platform toward one of the stable equilibria.

The energy harvester with a bistable structure has two motion patterns: intrawell oscillations and interwell oscillations. The intrawell oscillations occur around one of the two stable equilibria, whereas the interwell oscillations can cross the unstable equilibrium twice per excitation cycle. More importantly, the interwell oscillations also include two vibration patterns, namely, interwell chaotic oscillations and interwell periodic motion, which are determined by the amplitude and frequency of excitation. The effect of the motion patterns on the energy harvesting performance is discussed below in detail.

Fig. 4 **a** Potential energy curves and **b** mechanical properties of the hybrid energy harvester for different γ



3 Analytical analysis

3.1 Dynamic analysis

It is convenient to consider the hybrid energy harvester proposed in this paper in terms of different mechanical systems, i.e., the linear system, conventional QZS (CQZS) system, dual QZS (DQZS) system, and bistable system. In this section, the electrical properties of the energy harvester are analysed. However, the analysis of the bistable system is not presented here, because it is difficult to derive an analytical result for the displacement and velocity responses in this type of system, as well as the electrical characteristics. Considering a base excitation $z(t) = Z \sin(\omega t)$ that is applied to the energy harvester, the equation of motion can be given by

$$M\ddot{y} + c\dot{y} + F = -MA \sin(\omega t) \tag{13}$$

where $A = Z\omega^2$ is the amplitude of the base acceleration, ω is the excitation frequency, and c is the total damping of the mechanical structure and electromagnetic system. K and M denote the stiffness of the vertical spring and the lumped mass of the energy harvester, respectively. Note that, the lumped mass of the platform is supported by the linear coil spring (positive stiffness mechanism) alone at the equilibrium position, enabling an outstanding carrying capacity of the energy harvester.

First, the mechanical structure of the energy harvester can be easily converted to a linear one by removing the negative stiffness mechanism. In this case, the expression for F in Eq. (13) is equal to Ky , and the expressions for the displacement and velocity are given as

$$y(t) = \frac{MA \sin(\omega t - \phi)}{\sqrt{(K - A)^2 + c^2\omega^2}} \tag{14}$$

$$v(t) = \dot{y}(t) = \frac{MA \cos(\omega t - \phi)}{\sqrt{(K - A)^2 + c^2\omega^2}} \tag{15}$$

where ϕ is the phase angle of the response.

When the permanent magnet rings are removed from the QZS spring, the energy harvester has a CQZS structure. The restoring force can be written as

$$F = K \left[y - \frac{by}{\delta} \left(\frac{\delta + b}{\sqrt{b^2 + y^2}} - 1 \right) \right] \tag{16}$$

The equation of motion for this CQZS system has been analysed by the harmonic balance method in previous works [44] and is written as

$$y(t) = Y \sin(\omega t - \phi) \tag{17}$$

$$v(t) = \dot{y}(t) = -Y\omega \cos(\omega t - \phi) \tag{18}$$

where Y denotes the response amplitude and can be calculated as [45]

$$\bar{\omega}_{1,2} = \frac{1}{2} \sqrt{3\chi\bar{Y}^2 - 8\zeta^2 \pm \frac{4}{\bar{Y}} \sqrt{4\zeta^4\bar{Y}^2 - 3\chi\bar{Y}^4\zeta^2 + \Xi^2}} \tag{19}$$

where $\bar{\omega} = \omega/\omega_0$ denotes the ratio of the excitation frequency to the natural frequency of the corresponding linear system. $\bar{Y} = Y/b$ denotes the dimensionless amplitude of the displacement response. χ is a nonlinear parameter of the stiffness of the energy harvester, $\zeta = c/2\sqrt{KM}$ is the damping ratio, and $\Xi = M_A/K_b$ is the dimensionless external load applied

to the energy harvester. For a given excitation, one can easily obtain the displacement response using Eq. (19).

As mentioned above, γ can be varied to change the structure of the energy harvester to one with a different mechanical mechanism. γ has the threshold value of 0.77, at which the energy harvester has a DQZS structure with a large displacement region in which the stiffness is close to zero. The corresponding restoring force, $F_{HEH,QZS}$, is given by Eq. (10), and the amplitude–frequency relationship is given by

$$\left(-\bar{\omega}^2 + \alpha_1 \bar{Y} + \frac{3}{4} \alpha_2 \bar{Y}^3 + \frac{5}{8} \alpha_3 \bar{Y}^5 + \frac{35}{64} \alpha_4 \bar{Y}^7\right)^2 + (2\zeta \bar{\omega} \bar{Y})^2 = \Xi^2 \tag{20}$$

where $\alpha_1 = 0.006$, $\alpha_2 = -0.45$, $\alpha_3 = 14.74$, and $\alpha_4 = -27.69$ are the coefficients for the x , x^3 , x^5 , and x^7 components, respectively, of the fitted polynomial. For a given excitation frequency, the dimensionless displacement response is easily obtained using Eq. (20).

The open-circuit voltage and short-circuit current of a TEG can be written as [46]

$$|V_{OC(TEG)}| = \frac{\sigma_{CD} y(t)}{\epsilon_0 [L - y(t)]} \left(\frac{d_1}{\epsilon_1} + \frac{d_2}{\epsilon_2} \right), \quad |y| \leq 0.9L \tag{21}$$

$$I_{SC(TEG)} = \sigma_{CD} w \frac{dx}{dt} = \sigma_{CD} w v(t) \tag{22}$$

where $y(t)$ and $v(t)$ denote the separation between the two friction surfaces and the sliding velocity of Dielectric 1, respectively; d_1 and d_2 denote the thicknesses of Dielectric 1 and Dielectric 2, respectively. L is the length of the dielectrics, σ_{CD} is the charge density of the dielectrics when they slide, and ϵ_1 and ϵ_2 are the relative permittivity of Dielectric 1 and Dielectric 2, respectively. ϵ_0 is the permittivity of free space, and w is the width of the dielectrics.

According to the literature [13], the open-circuit voltage produced by the EMG can be written as

$$V_{OC(EEH)} = NBL_{EMG}v(t) \tag{23}$$

where B and N denote the magnetic field strength and number of coil turns, respectively, and L_{EMG} represents the length of each coil. In addition, the short-circuit current of the EMG is given by

$$I_{SC(EEH)} = \frac{NBL_{EMG}v(t)}{R_L} \tag{24}$$

where R_L denotes the total coil resistance.

3.2 Jump phenomena

Figure 5 shows the analytical results for the open-circuit voltage of the TEG and EMG calculated using the parameters listed in Table 2. Note that the black, blue, and red lines denote the open-circuit voltages of the DQZS, CQZS, and linear energy harvesters, respectively. Clearly, compared with the CQZS and linear TEGs, the DQZS TEG exhibits the highest open-circuit voltage owing to its low resonant frequency. The peak open-circuit voltage of the DQZS EMG is approximately equal to that produced by a CQZS. However, the excitation frequency of the DQZS EMG corresponding to the maximum open-circuit voltage is lower than that of the CQZS EMG, about 4 Hz.

Figure 6 shows the analytical short-circuit currents of the TEG and EMG in each mechanical system. The lines have the same meanings as in Fig. 5. A comparison of Figs. 5 and 6 reveals that the short-circuit currents of the TEG and EMG exhibit the same trend as the open-circuit voltages for each mechanical system. However, the peak short-circuit currents of the DQZS and CQZS are approximately equal, which is different from the open-circuit voltages of the TEG.

3.3 Numerical simulations

The analytical approach is convenient and can accurately predict the electrical outputs for a small-amplitude excitation. However, when the excitation amplitude increases, resulting in strong nonlinearity, the analytical method cannot accurately predict the energy harvesting efficiency of the system. In addition, when the mechanical structure becomes bistable, the analytical method also fails. Therefore, to overcome this shortcoming of the analytical approach and to validate the analytical results, the equation of motion of the energy harvester with the original nonlinear stiffness is solved by a numerical method in this section. The numerical electrical outputs of the energy harvester are also obtained.

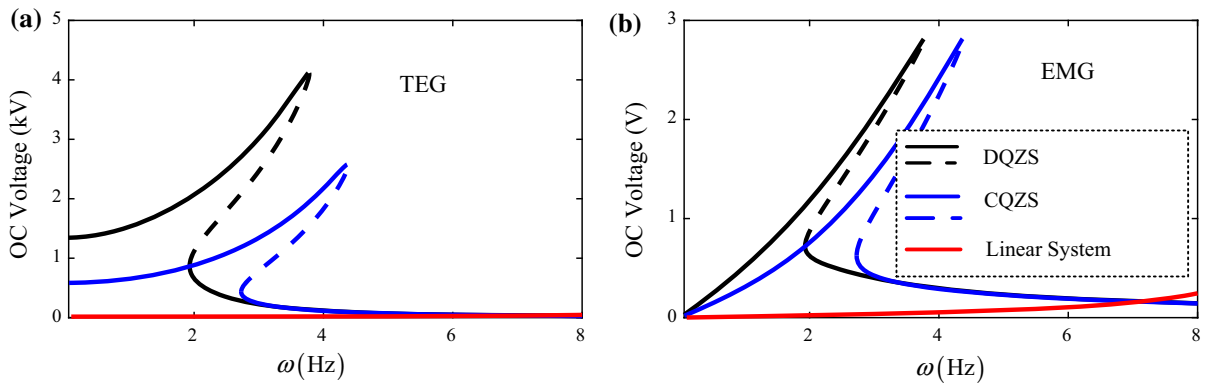


Fig. 5 Analytical results for the open-circuit voltage of **a** the TEG and **b** the EMG for different mechanical systems at an acceleration amplitude of 2 g. Black, blue, and red lines

represent the DQZS, CQZS, and linear systems, respectively. Dashed lines denote the unstable solutions

Table 2 Numerical simulation parameters of the devised hybrid energy harvester

Parameter	Value
Dielectric 1	$\epsilon_{r1} = 4, d_1 = 2.2 \times 10^{-4} \text{ m}$
Dielectric 2	$\epsilon_{r2} = 2, d_2 = 2.2 \times 10^{-2} \text{ m}$
Width of the dielectrics	$w = 0.04 \text{ m}$
Length of the dielectrics	$L = 0.045 \text{ m}$
Surface tribo-charge density	$\sigma_{CD} = 80 \mu\text{C}/\text{m}^2$
Permittivity of free space	$\epsilon_0 = 8.85 \times 10^{-12} \text{ F}/\text{m}$
Magnetic field strength (at 1.5 mm distance)	$B = 0.45 \text{ T}$
Length of coil	$L_{EMG} = 10 \text{ mm}$
Number of coil turns	$N = 800$
Total coil resistance	$R_L = 128 \Omega$

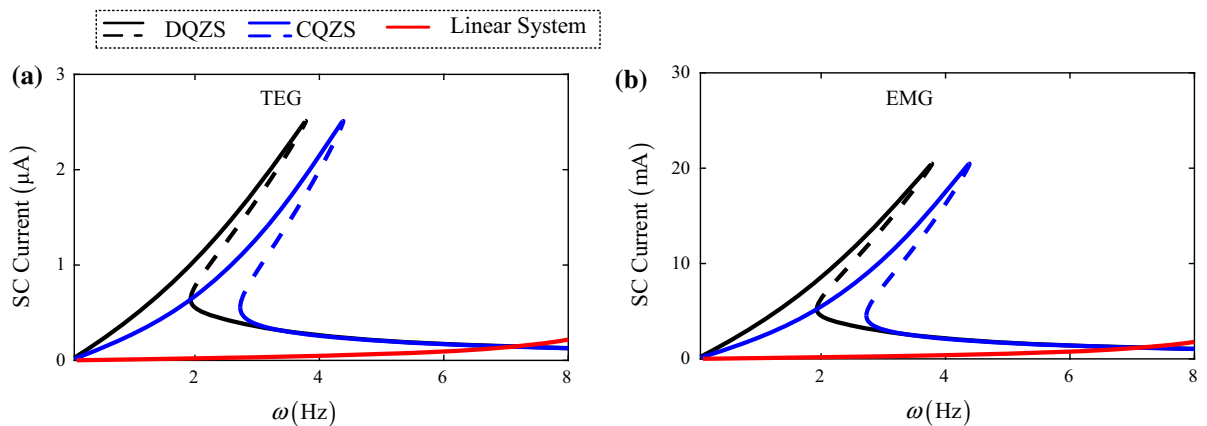


Fig. 6 Analytical results for the short-circuit currents of **a** the TEG and **b** the EMG for different mechanical systems at an acceleration amplitude of 2 g

3.4 Verification of the analytical results

Figure 7 shows the numerically obtained electrical characteristics (including the open-circuit voltage and short-circuit current) of the TEG for different mechanical systems and excitation frequencies. Panels (a), (b), and (c) show the electrical outputs of the linear, CQZS, and DQZS TEGs, respectively. A comparison of Figs. 5a and 6a reveals that the numerically obtained open-circuit voltage and short-circuit current of the

TEG at an excitation amplitude of 2 g are in excellent agreement with the analytical results. As the excitation frequency increases, the peak values of the open-circuit voltage and short-circuit current of the linear TEG clearly increase monotonically in the given frequency range. For the CQZS and DQZS TEGs, however, both the open-circuit voltage and short-circuit current first increase monotonically to the peak value and then decrease sharply. That is, a jump-down phenomenon also appears in the electrical outputs.

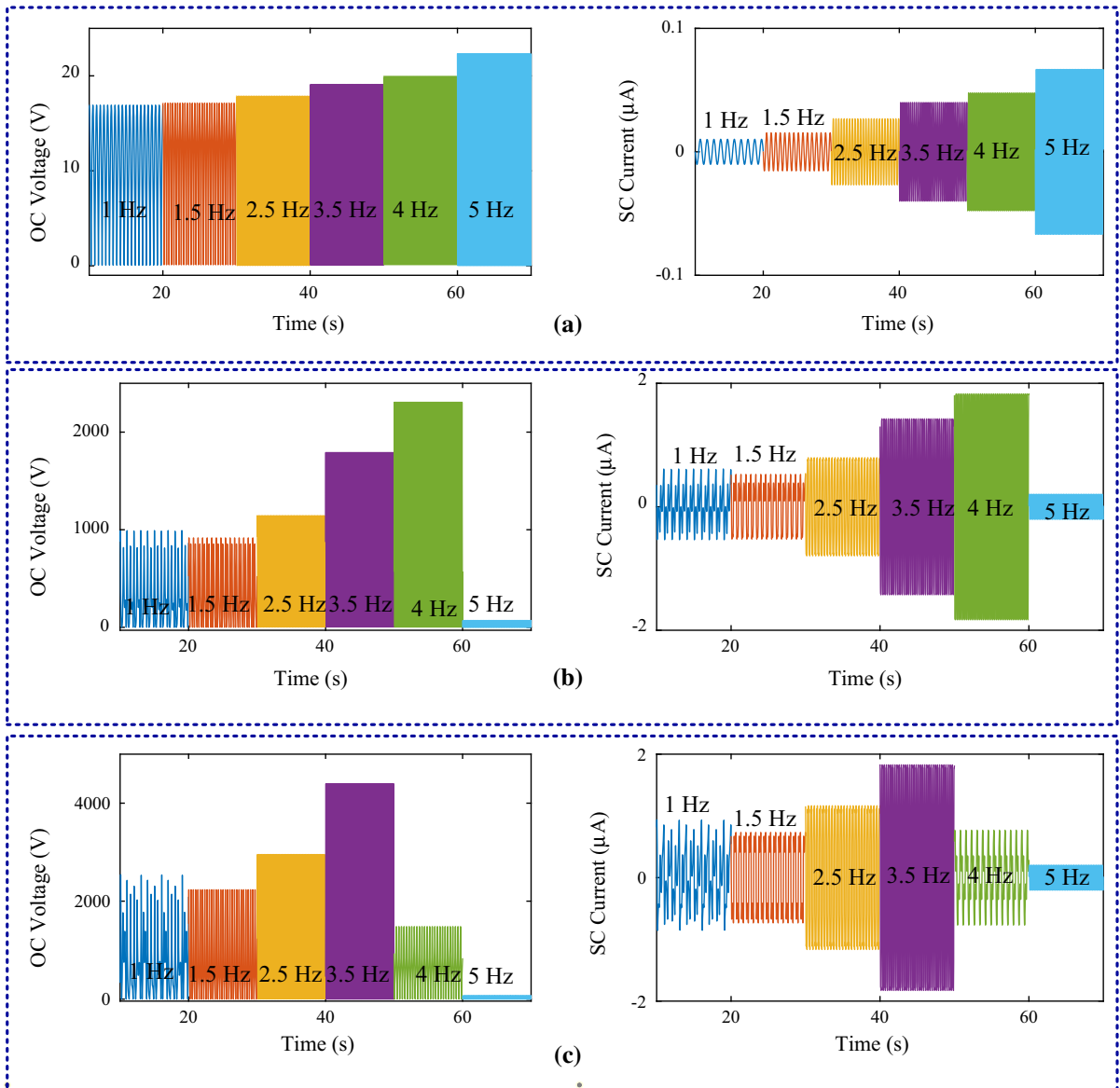


Fig. 7 Numerical results for the open-circuit voltage and short-circuit current of the TEG for different mechanical systems. **a** Linear system, **b** CQZS system, and **c** DQZS system

Figure 8 shows the time series of the open-circuit voltage and short-circuit current of the EMG for different mechanical systems and excitation frequencies. The excitation amplitude is 2 g. Before the excitation frequency reaches the jump-down frequency, the open-circuit voltage and short-circuit current both clearly increase with increasing excitation frequency, but they decrease sharply when the

excitation frequency matches the jump-down frequency. A comparison of Figs. 5b, 6b, and 8 reveals that the theoretical and numerical results are in excellent agreement. Therefore, the analytical approach using the harmonic balance method can accurately predict the energy harvesting performance at ultralow frequencies.

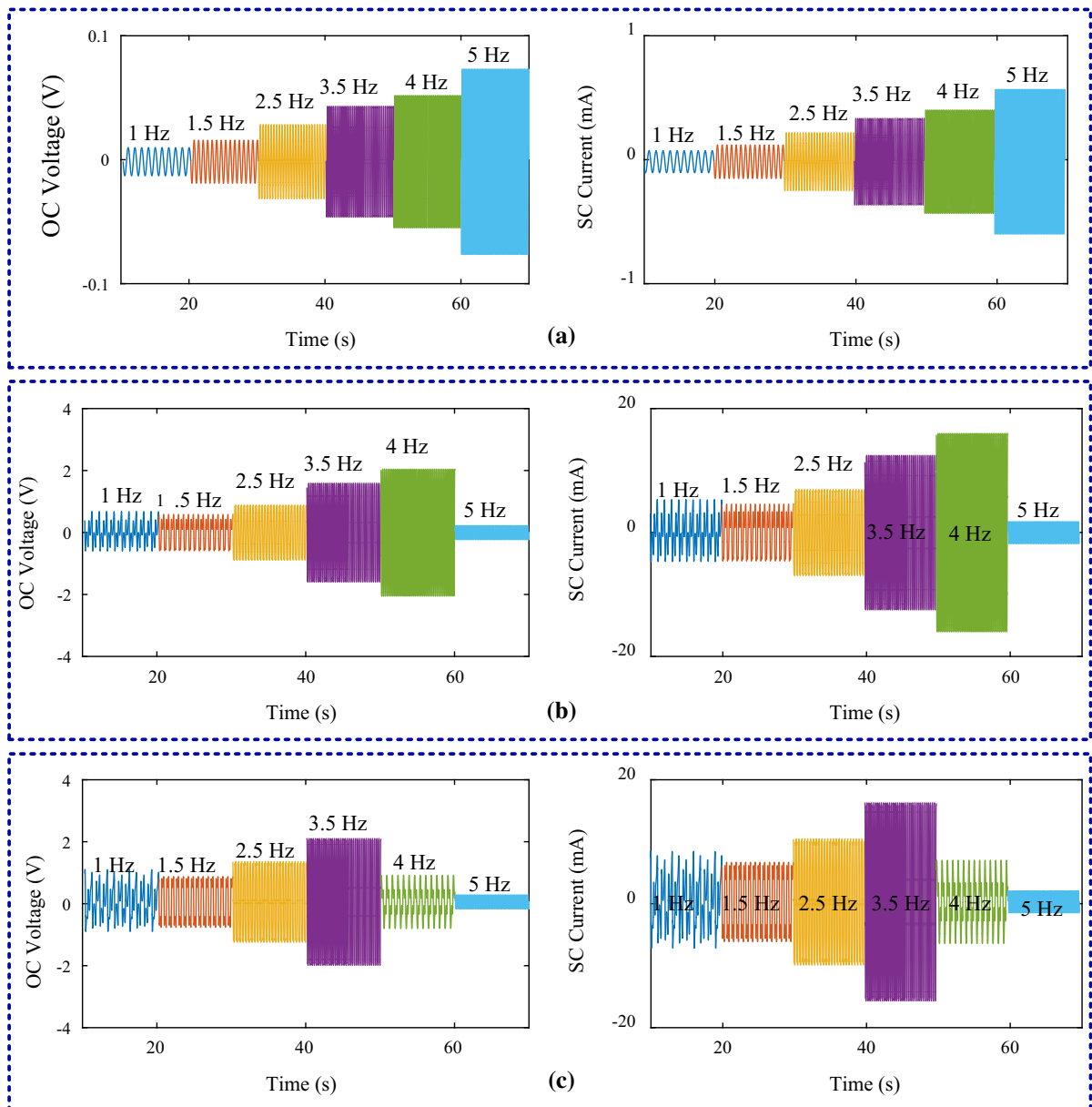


Fig. 8 Numerical results for the open-circuit voltage and short-circuit current of the EMG for different mechanical systems. **a** Linear system, **b** CQZS system, and **c** DQZS system

As mentioned in Sect. 2, when the stiffness ratio γ is less than the threshold of 0.77, the energy harvester becomes a bistable system. Figure 9 shows the open-circuit voltage and short-circuit current of the energy harvester for $\gamma = 0.4$. The bistable energy harvester clearly converts the ultralow-frequency mechanical energy more efficiently than the other systems. Specifically, the bistable TEG produces an open-circuit voltage of 7.47 kV and a short-circuit current of 1.53 μA at an excitation frequency of 2.5 Hz. Clearly, these electrical outputs are superior to those generated by the linear TEG, CQZS TEG, and even the DQZS TEG in this low-frequency range. Figure 9b shows the electrical features of the bistable EMG at different excitation frequencies. Unlike the results for the other three systems, the excitation frequency corresponding to the peak open-circuit voltage and the peak short-circuit current are lower. In fact, the improvement in the electrical characteristics of the bistable EMG is similar to that of the bistable TEG and results from the large dynamic response at low frequency.

3.5 Nonlinear electrical characteristics

For a sliding-mode TEG, the approximate V - Q - y relationship can be written as [40]

$$V(t) = -\frac{Q(t)}{w\varepsilon_0[L-y(t)]} \left(\frac{d_1}{\varepsilon_1} + \frac{d_2}{\varepsilon_2} \right) + \frac{\sigma_{CD}y(t)}{\varepsilon_0[L-y(t)]} \left(\frac{d_1}{\varepsilon_1} + \frac{d_2}{\varepsilon_2} \right) \tag{25}$$

where Q is the total charge transferred between the electrodes. When a load resistance is introduced into the TEG, according to Ohm’s law, the output current and voltage are expressed as

$$V(t) = I(t) \cdot R = R \frac{dQ(t)}{dt} \tag{26}$$

By combining Eqs. (26) and (25), the nonlinear relationship between the geometrical and electrical parameters can be expressed as

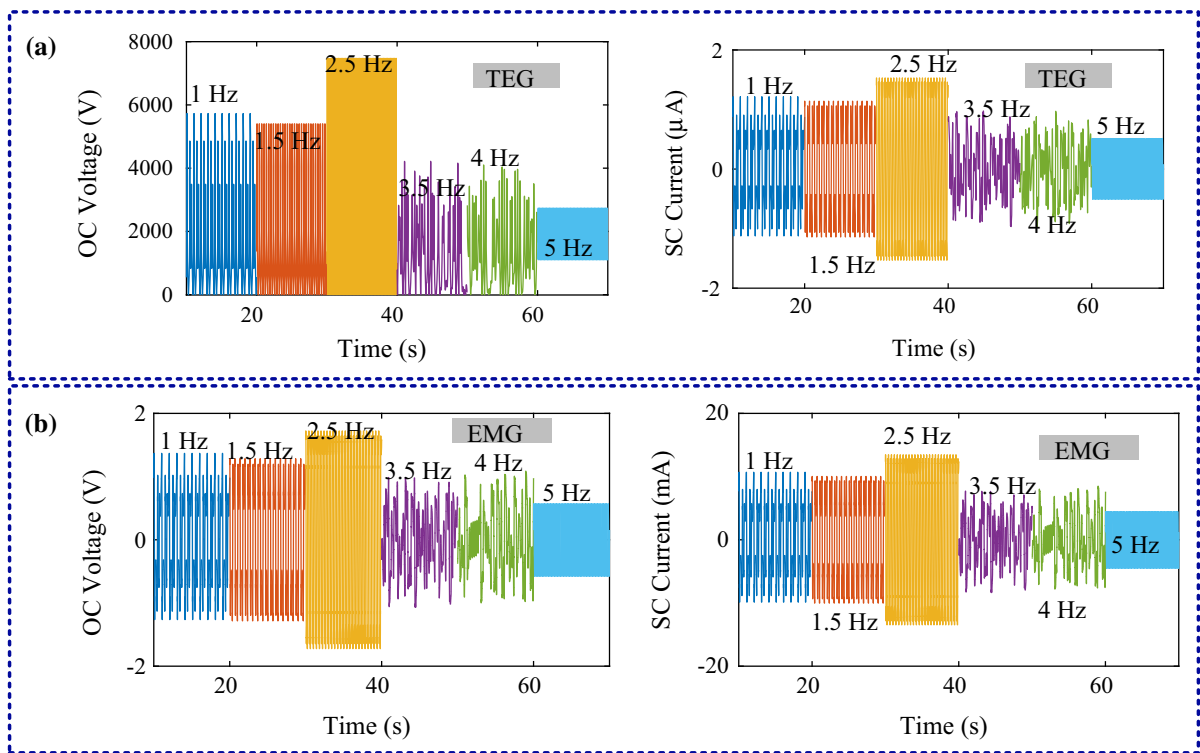


Fig. 9 Numerical results for the open-circuit voltage and short-circuit current for **a** the bistable TEG and **b** the bistable EMG

$$R \frac{dQ(t)}{dt} = -\frac{Q(t)}{w\epsilon_0[L-y(t)]} \left(\frac{d_1}{\epsilon_{r1}} + \frac{d_2}{\epsilon_{r2}} \right) + \frac{\sigma_{CD}y(t)}{\epsilon_0[L-y(t)]} \left(\frac{d_1}{\epsilon_{r1}} + \frac{d_2}{\epsilon_{r2}} \right) \quad (27)$$

The output electrical performance of the sliding-mode TEG, including the output current, voltage, and power, can be evaluated by solving the electrical and dynamic equations using the Runge–Kutta method.

Figure 10 compares the numerical electrical features of the energy harvester with the linear, QZS, and

bistable systems at an excitation frequency of 3.5 Hz and an excitation amplitude of 2 g. ‘C-’ and ‘P-’ denote the peak values of the output current and output power, respectively, of the energy harvesters.

Figure 10a, c show the numerically obtained electrical outputs of the linear, CQZS, and DQZS EMGs. With increasing load resistance, the output current clearly decreases continuously, but the output power increases to a maximum and then decreases. In addition, the linear EMG exhibits the worst electrical performance among the three mechanical systems. By

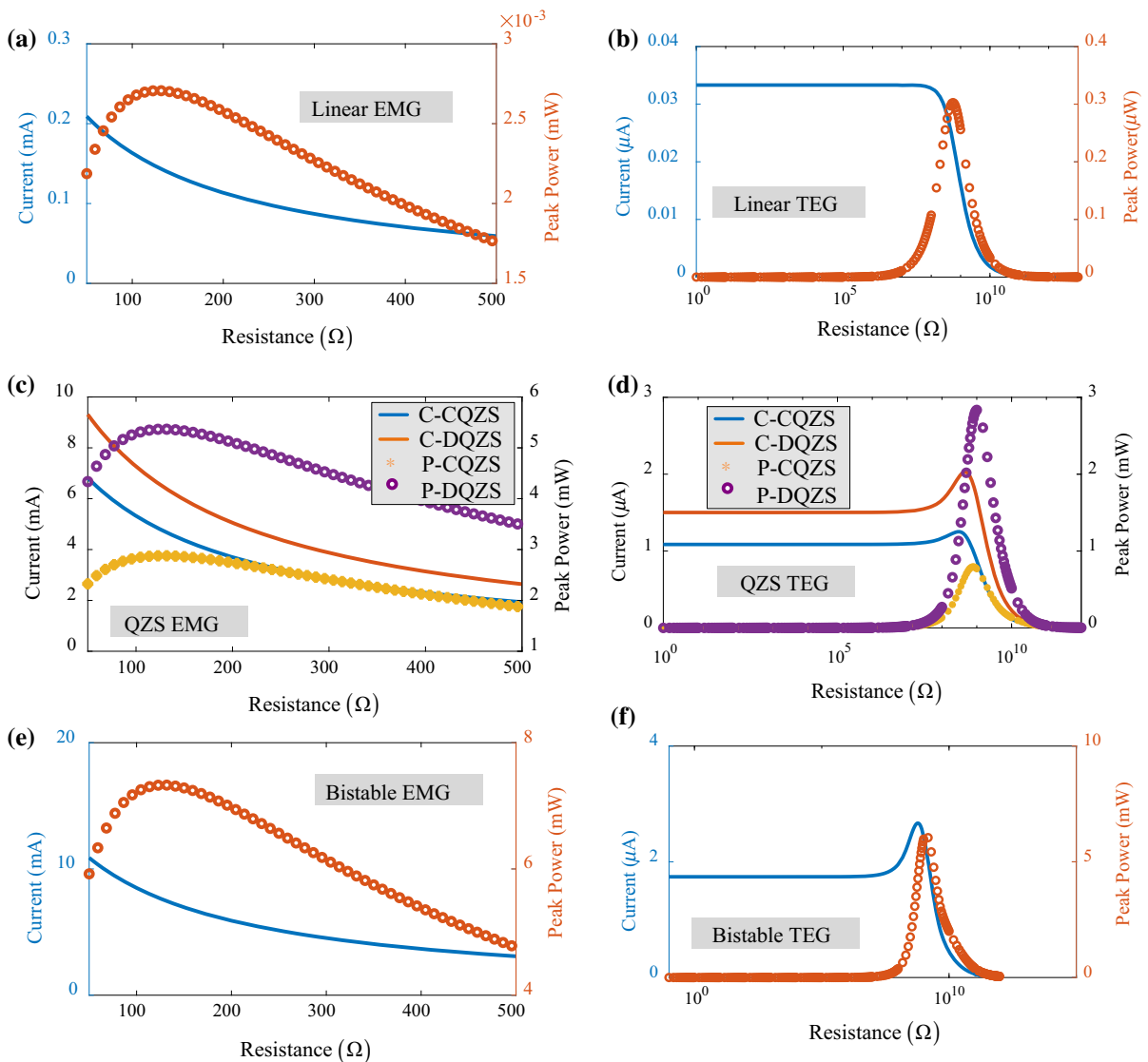


Fig. 10 Numerical results for the output current and corresponding power of **a** and **b** linear EMG and TEG, **c** and **d** QZS EMG and TEG, **e** and **f** bistable EMG and TEG ($\gamma=0.5$). The

excitation frequency is 3 Hz, and the excitation amplitude is 2 g. ‘C-’ and ‘P-’ denote the peak values of the output current and output power, respectively

contrast, the DQZS EMG generates the maximum output voltage and maximum output power, as indicated by the orange dotted and solid lines, respectively, in Fig. 10c. In fact, the electrical performance of the EMG can be attributed to the differences in the dynamic response (including the displacement response and velocity response) produced by the energy harvester. As mentioned above, the dynamic response is related to the natural frequency of the linear and QZS energy harvesters, and the distance between the two equilibria of the bistable energy harvester. When the excitation frequency is close to the natural frequency, or the excitation forces the energy harvester to cross the potential barrier, the system produces a dynamic displacement and velocity response with large amplitude.

Figure 10b, d show the output current and output power of the three different types of TEG under different load resistances. Like the linear EMG, the linear TEG exhibits the worst energy harvesting performance, and the DQZS TEG exhibits the best performance. The two types of energy harvester differ in the optimal load resistance corresponding to the best energy conversion performance. Specifically, the optimal load resistance of the EMG is approximately 127.3Ω , but that of the TEG is approximately $1.5 \times 10^9 \Omega$.

In addition, the behaviour of the output current of the TEG differs from that of the EMG. Specifically, the output current of the linear TEG remains unchanged and is close to the short-circuit current when the load resistance is less than the optimal one. When the load resistance exceeds the optimal value, the output current decreases sharply and approaches zero as the load resistance increases further. For the CQZS and DQZS TEGs (Fig. 10d), with increasing load resistance, the output current initially remains stable and then reaches a peak value and decreases sharply. In fact, the plateau in the output current can be attributed to the fact that the increase speed of the voltage peak value is greater than that of the load resistance [40].

More importantly, with increasing load resistance, the output power increases slowly when the resistance is much lower than the optimal value. However, when the resistance is close to the optimal value, the output power increases sharply and then reaches a peak at the optimal resistance. When the resistance increases

beyond the optimal value, the output power decreases sharply and approaches zero.

The output current and power of the bistable EMG and TEG are shown in Fig. 10e, f, respectively. Compared with the QZS energy harvesters, the bistable energy harvesters convert the ultralow frequency vibration energy more efficiently, with a peak power of 7.33 mW for the EMG and 6.04 mW for the TEG. In fact, the better energy harvesting performance of the bistable mechanical system can be attributed to the fact that the bistable mechanism induces periodic interwell (also called snap-through) oscillations with a large amplitude displacement and velocity.

3.6 Nonlinear dynamics of the hybrid energy harvester

Figure 11 illustrates the motion patterns of the energy harvester under different excitation amplitudes and excitation frequencies. The green, yellow, light blue, and dark blue regions indicate areas of interwell periodic oscillation, interwell aperiodic/chaotic oscillations, intrawell aperiodic oscillations, and intrawell periodic oscillations, respectively. There is a threshold value of the excitation amplitude for each excitation frequency at which the motion pattern switches from intrawell oscillation to interwell oscillation. In addition, it is noteworthy that there may not be a clear boundary between the two motion patterns, for example, in region 4, where interwell aperiodic/chaotic oscillations and interwell periodic oscillations are intermixed. The interwell aperiodic/chaotic oscillations and intrawell aperiodic oscillations are intermixed in region 2. The low-frequency energy harvesting performance of each of the motion patterns of the energy harvester is analysed below.

To analyse the effect of the excitation frequency on the energy harvesting performance of the energy harvester, the influence of the excitation frequency on the motion pattern is first analysed. Figure 12 shows the response of the energy harvester for a stiffness ratio of $\gamma=0.5$ and an excitation amplitude of $A = 2 \text{ g}$. At all of these excitation frequencies, the fundamental motion pattern is large-amplitude interwell oscillation. With increasing excitation frequency, the peak values of both the displacement response and velocity amplitude increase. However, when the excitation frequency exceeds a threshold, for example, 4 Hz in Fig. 12d, the motion of the hybrid energy harvester

Fig. 11 Motion patterns of the energy harvester under different excitation frequencies and excitation amplitudes for a stiffness ratio of 0.5

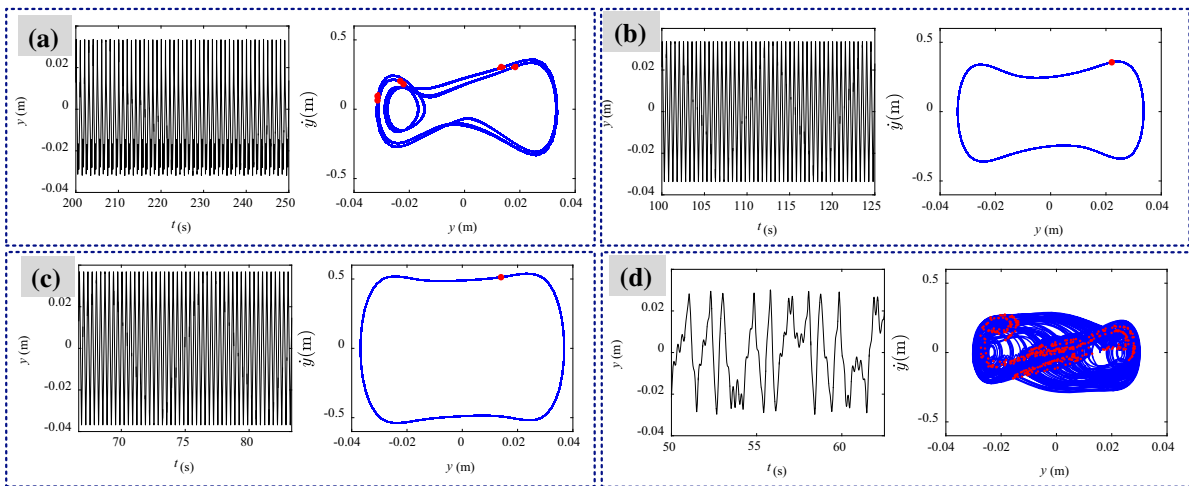
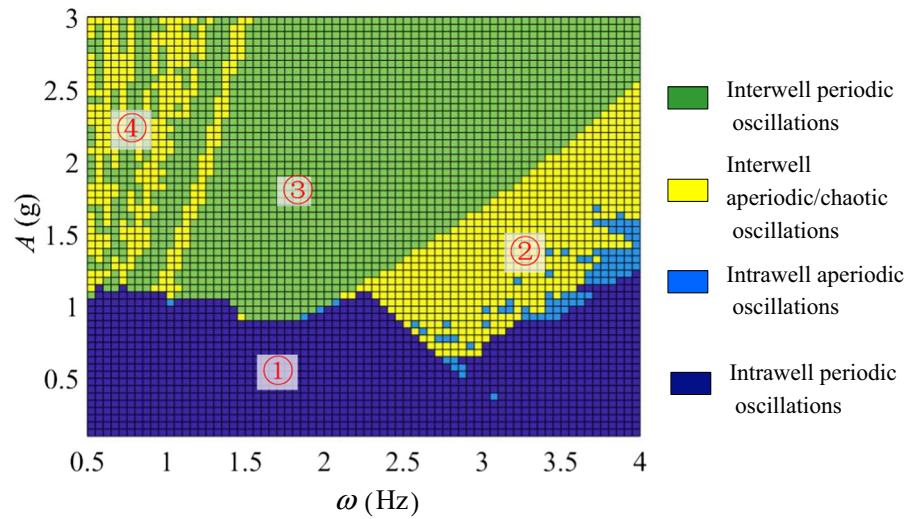


Fig. 12 Response of the energy harvester at an excitation amplitude of $A = 2$ g, a stiffness ratio of $\gamma=0.5$, and an excitation frequency of **a** $\omega=1$ Hz, **b** $\omega = 2$ Hz, **c** $\omega=3$ Hz, **d** $\omega=4$ Hz

switches from interwell periodic oscillation to interwell aperiodic/chaotic oscillation; consequently, both the displacement amplitude and velocity amplitude decrease.

The effect of the excitation frequency on the root-mean-square (RMS) output power is shown in Fig. 13. Clearly, the output power of both the EMG and TEG increases with increasing excitation frequency and then decreases sharply when the excitation frequency exceeds a threshold. Specifically, the EMG and TEG with bistable structure produce the maximum output power when the excitation frequency is equal to the threshold value; this behaviour is identical to the

jump-down phenomenon in nonlinear systems such as the CQZS system. In fact, as mentioned above, the fundamental reason for this variation in the output power is that increasing the excitation frequency causes the motion pattern to switch from interwell periodic oscillation to aperiodic/chaotic oscillation. Consequently, the response amplitude decreases, and the ultralow-frequency vibration energy conversion is degraded.

Figure 14 shows the effect of the stiffness ratio on the motion pattern of the energy harvester. When the stiffness ratio is 0.1, as shown in Fig. 14a, the energy harvester cannot cross the potential barrier induced by

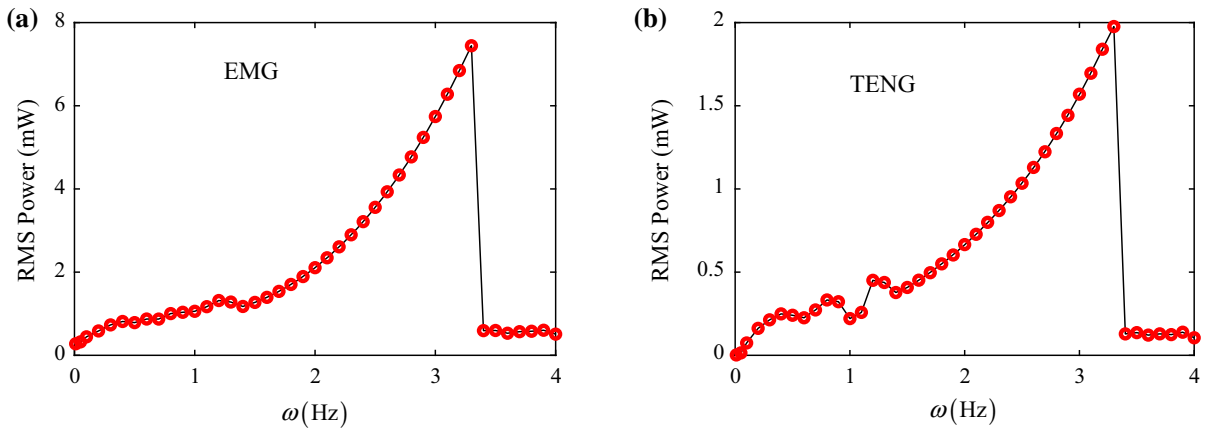


Fig. 13 Numerical RMS of output power of **a** EMG and **b** TENG at a stiffness ratio of $\gamma=0.5$ and an excitation amplitude of $A = 2$ g

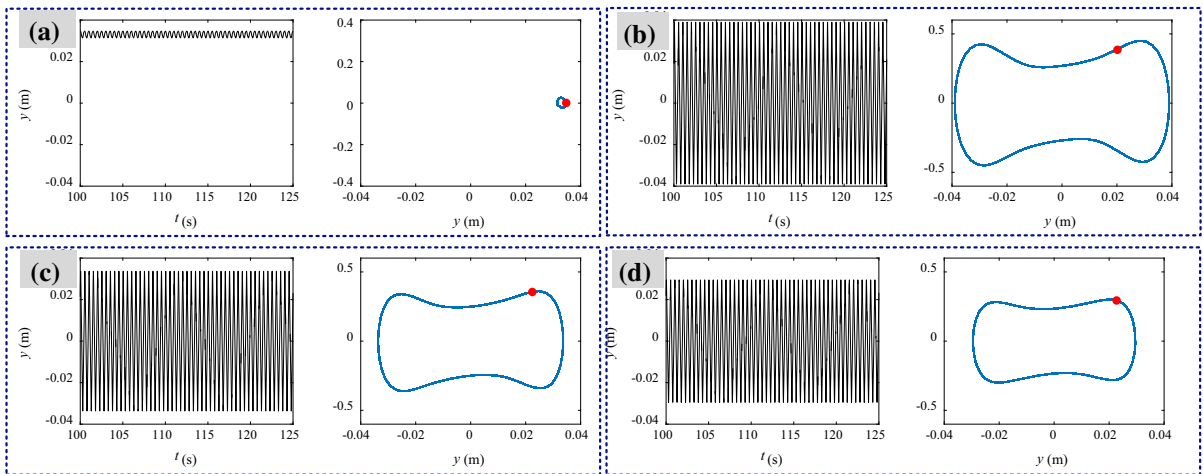


Fig. 14 Motion patterns induced by bistable structure for an excitation frequency of $\omega=2$ Hz, an excitation amplitude of $A = 2$ g, and a stiffness ratio of **a** $\gamma = 0.1$, **b** $\gamma = 0.3$, **c** $\gamma = 0.5$, and **d** $\gamma = 0.7$

the negative stiffness mechanism. It oscillates at one of the stable equilibria with a small dynamic response amplitude. For this motion pattern, the energy harvester cannot convert the ultralow frequency vibration energy effectively.

For a stiffness ratio of 0.3 (Fig. 14b), the energy harvester oscillates periodically between two wells. The response amplitude is larger than that of the intrawell periodic oscillations in Fig. 14a. At stiffness ratios of 0.5 and 0.7, as shown in Fig. 14c, d, respectively, the phase diagram of the energy harvester has an almost elliptical profile, and the dynamic response amplitude gradually decreases. Therefore, the stiffness ratio is important for improving the

energy harvesting performance for ultralow frequency vibrations.

Figure 15 shows the effect of the stiffness ratio on the RMS output power of the energy harvester at an excitation frequency of 2 Hz and an excitation amplitude of 2 g. Note that as the stiffness ratio decreases, the potential barrier of the bistable energy harvester can increase significantly, resulting in intrawell oscillation and mediocre energy harvesting performance for ultralow frequency vibration. However, increasing the stiffness ratio could decrease the distance between the two stable equilibria, which also degrades the energy conversion. More importantly, the bistable energy harvester becomes a DQZS system when $\gamma = 0.77$ and a CQZS system when $\gamma > 0.77$. According to

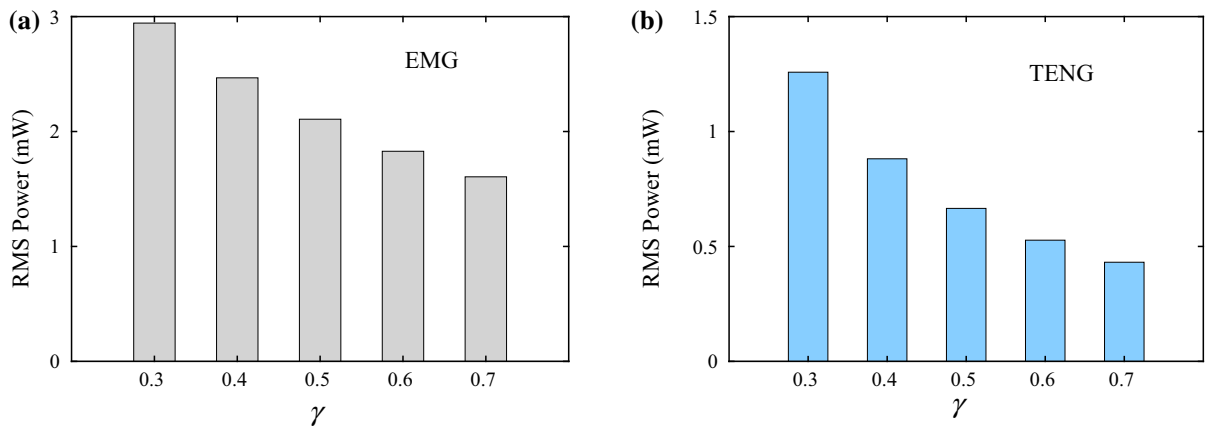


Fig. 15 Numerically obtained RMS output power of **a** EMG and **b** TEG at different stiffness ratios for a driving frequency of $\omega=2$ Hz and an external excitation amplitude of $A = 2$ g

the above analysis, the energy harvesting performance of the QZS system cannot exceed that of the bistable system. Therefore, a suitable γ value should be chosen to convert the ultralow-frequency vibration energy efficiently.

As shown in Fig. 15a, as the stiffness ratio increases, the RMS power of the EMG decreases monotonously from 2.95 to 1.61 mW. The RMS power of the TEG (Fig. 15b) is similar to that of the EMG with increasing stiffness ratio; it decreases from 1.26 to 0.43 mW. Therefore, it is best to design an energy harvesting system with a low stiffness ratio to harvest the ultralow frequency vibration energy. However, as mentioned above, as the stiffness ratio decreases, the potential barrier could increase significantly, and a large-amplitude excitation is needed for the energy harvester to cross the potential barrier.

4 Conclusions

This paper proposes a nonlinear hybrid energy harvester containing an EMG and a TEG to improve the energy harvesting performance at ultralow frequencies. The mechanical configuration of the energy harvester includes a linear spring and four QZS springs that provide negative stiffness along the vertical direction. According to the parametric design, the energy harvester shows different mechanical behaviour, including linear, CQZS, DQZS, and bistable systems. The energy harvesting performance of the linear and QZS systems is analysed theoretically

and verified numerically. The electrical outputs of the bistable energy harvester are also obtained using a numerical method. The conclusions are as follows.

- (1) The DQZS system has a larger low-stiffness displacement region than the CQZS system, and the energy harvester has a large-amplitude response and thus better energy harvesting performance at ultralow frequencies.
- (2) Among the four mechanical systems, the linear system exhibits the worst energy harvesting performance, and the bistable system exhibits the best performance for both the EMG and TEG under an excitation with the same amplitude and frequency.
- (3) According to the dynamical response of the nonlinear system, the energy harvesting performance improves with increasing excitation frequency until it reaches a maximum at the threshold frequency. When the excitation frequency exceeds the threshold value, the energy harvesting performance degrades considerably.

Acknowledgements This research work was supported by China Postdoctoral Science Foundation (2020M672476), National Natural Science Foundation of China (12002122, 11972152) and National Key R&D Program of China (2017YFB1102801). The first author, Kai Wang, would like to thank the support from the China Scholarship Council (CSC) which sponsors his visit to the University of Liverpool where the original idea was conceived.

Compliance with ethical standards

Conflict of interest The authors declare no conflict of interest.

References

- Schaller RD, Klimov VI (2004) High efficiency carrier multiplication in PbSe nanocrystals: implications for solar energy conversion. *Phys Rev Lett* 92:1–4. <https://doi.org/10.1103/physrevlett.92.186601>
- Träsch M, Déporte A, Delacroix S et al (2019) Analytical linear modelization of a buckled undulating membrane tidal energy converter. *Renew Energy* 130:245–255. <https://doi.org/10.1016/j.renene.2018.06.049>
- Chen BD, Tang W, He C et al (2018) Water wave energy harvesting and self-powered liquid-surface fluctuation sensing based on bionic-jellyfish triboelectric nanogenerator. *Mater Today* 21:88–97. <https://doi.org/10.1016/j.mattod.2017.10.006>
- Kammer AS, Olgac N (2016) Delayed-feedback vibration absorbers to enhance energy harvesting. *J Sound Vib* 363:54–67. <https://doi.org/10.1016/j.jsv.2015.10.030>
- Castagnetti D (2019) A simply tunable electromagnetic pendulum energy harvester. *Meccanica* 54:749–760. <https://doi.org/10.1007/s11012-019-00976-7>
- Halim MA, Rantz R, Zhang Q et al (2018) An electromagnetic rotational energy harvester using sprung eccentric rotor, driven by pseudo-walking motion. *Appl Energy* 217:66–74. <https://doi.org/10.1016/j.apenergy.2018.02.093>
- Qiu GL, Liu W, Di Han M et al (2015) A cubic triboelectric generator as a self-powered orientation sensor. *Sci China Technol Sci* 58:842–847. <https://doi.org/10.1007/s11431-015-5790-7>
- Litak G, Friswell MI, Adhikari S (2016) Regular and chaotic vibration in a piezoelectric energy harvester. *Meccanica* 51:1017–1025. <https://doi.org/10.1007/s11012-015-0287-9>
- Yang Y, Guo W, Pradel KC et al (2012) Pyroelectric nanogenerators for harvesting thermoelectric energy. *Nano Lett* 12:2833–2838. <https://doi.org/10.1021/nl3003039>
- Siang J, Lim MH, Leong MS (2018) Review of vibration-based energy harvesting technology: mechanism and architectural approach. *Int J Energy Res* 42:1866–1893. <https://doi.org/10.1002/er.3986>
- Naifar S, Bradai S, Viehweger C, Kanoun O (2017) Survey of electromagnetic and magnetoelectric vibration energy harvesters for low frequency excitation. *Measurement* 106:251–263. <https://doi.org/10.1016/j.measurement.2016.07.074>
- Fan K, Cai M, Liu H, Zhang Y (2019) Capturing energy from ultra-low frequency vibrations and human motion through a monostable electromagnetic energy harvester. *Energy* 169:356–368. <https://doi.org/10.1016/j.energy.2018.12.053>
- Halim MA, Cho H, Park JY (2015) Design and experiment of a human-limb driven, frequency up-converted electromagnetic energy harvester. *Energy Convers Manag* 106:393–404. <https://doi.org/10.1016/j.enconman.2015.09.065>
- Zhu H, Li Y, Shen W, Zhu S (2019) Mechanical and energy-harvesting model for electromagnetic inertial mass dampers. *Mech Syst Signal Process* 120:203–220. <https://doi.org/10.1016/j.ymssp.2018.10.023>
- Yang B, Lee C, Xiang W et al (2009) Electromagnetic energy harvesting from vibrations of multiple frequencies. *J Micromechanics Microengineering* 19:035001. <https://doi.org/10.1088/0960-1317/19/3/035001>
- Muhammad F, Ket C, Ooi L, Yurchenko D (2019) Increased power output of an electromagnetic vibration energy harvester through anti-phase resonance. *Mech Syst Signal Process* 116:129–145. <https://doi.org/10.1016/j.ymssp.2018.06.012>
- Liu X, Qiu J, Chen H et al (2015) Design and optimization of an electromagnetic vibration. *IEEE Trans Magn* 51:1–4. <https://doi.org/10.1109/TMAG.2015.2437892>
- Zhang LB, Dai HL, Yang YW, Wang L (2019) Design of high-efficiency electromagnetic energy harvester based on a rolling magnet. *Energy Convers Manag* 185:202–210. <https://doi.org/10.1016/j.enconman.2019.01.089>
- Castagnetti D, Radi E (2018) A piezoelectric based energy harvester with dynamic magnification: modelling, design and experimental assessment. *Meccanica* 53:2725–2742. <https://doi.org/10.1007/s11012-018-0860-0>
- Castagnetti D (2015) A Belleville-spring-based electromagnetic energy harvester. *Smart Mater Struct* 24:94009. <https://doi.org/10.1088/0964-1726/24/9/094009>
- Fan F, Tian Z, Lin Z (2012) Flexible triboelectric generator! *Nano Energy* 1:328–334. <https://doi.org/10.1016/j.nanoen.2012.01.004>
- Wang S, Lin L, Xie Y et al (2013) Sliding-triboelectric nanogenerators based on in-plane charge-separation mechanism. *Nano Lett* 13:2226–2233. <https://doi.org/10.1021/nl400738p>
- He C, Zhu W, Gu GQ et al (2017) Integrative square-grid triboelectric nanogenerator as a vibrational energy harvester and impulsive force sensor. *Nano Res* 11:1157–1164. <https://doi.org/10.1007/s12274-017-1824-8>
- Bhatia D, Kim W, Lee S et al (2017) Tandem triboelectric nanogenerators for optimally scavenging mechanical energy with broadband vibration frequencies. *Nano Energy* 33:515–521. <https://doi.org/10.1016/j.nanoen.2017.01.059>
- Wu C, Liu R, Wang J et al (2017) A spring-based resonance coupling for hugely enhancing the performance of triboelectric nanogenerators for harvesting low-frequency vibration energy. *Nano Energy* 32:287–293. <https://doi.org/10.1016/j.nanoen.2016.12.061>
- Fu Y, Ouyang H, Davis RB (2020) Effects of electrical properties on vibrations via electromechanical coupling in triboelectric energy harvesting. *J Phys D Appl Phys* 53:215501. <https://doi.org/10.1088/1361-6463/ab7792>
- Huang X, Li L, Zhang Y (2013) Modeling the open circuit output voltage of piezoelectric nanogenerator. *Sci China Technol Sci* 56:2622–2629. <https://doi.org/10.1007/s11431-013-5352-9>
- Salaudin M, Toyabur RM, Maharjan P, Park JY (2018) High performance human-induced vibration driven hybrid energy harvester for powering portable electronics. *Nano Energy* 45:236–246. <https://doi.org/10.1016/j.nanoen.2017.12.046>

29. Fezeu GJ, Fokou ISM, Buckjohn CND et al (2020) Probabilistic analysis and ghost-stochastic resonance of a hybrid energy harvester under Gaussian White noise. *Meccanica* 55:1679–1691. <https://doi.org/10.1007/s11012-020-01204-3>
30. Fu Y, Ouyang H, Davis RB (2018) Nonlinear dynamics and triboelectric energy harvesting from a three-degree-of-freedom vibro-impact oscillator. *Nonlinear Dyn* 92:1985–2004. <https://doi.org/10.1007/s11071-018-4176-3>
31. Wang J, Geng L, Yang K et al (2020) Dynamics of the double-beam piezo–magneto–elastic nonlinear wind energy harvester exhibiting galloping-based vibration. *Nonlinear Dyn* 100:1963–1983. <https://doi.org/10.1007/s11071-020-05633-3>
32. Wang K, Zhou J, Chang Y et al (2020) A nonlinear ultralow-frequency vibration isolator with dual quasi-zero-stiffness mechanism. *Nonlinear Dyn* 101:755–773. <https://doi.org/10.1007/s11071-020-05806-0>
33. Sun X, Jing X (2015) Multi-direction vibration isolation with quasi-zero stiffness by employing geometrical nonlinearity. *Mech Syst Signal Process* 62:149–163. <https://doi.org/10.1016/j.ymssp.2015.01.026>
34. Hao Z, Cao Q, Wiercigroch M (2017) Nonlinear dynamics of the quasi-zero-stiffness SD oscillator based upon the local and global bifurcation analyses. *Nonlinear Dyn* 87:987–1014. <https://doi.org/10.1007/s11071-016-3093-6>
35. Wang K, Zhou J, Wang Q et al (2019) Low-frequency band gaps in a metamaterial rod by negative-stiffness mechanisms: design and experimental validation. *Appl Phys Lett* 114:251902. <https://doi.org/10.1063/1.5099425>
36. Wang K, Zhou J, Xu D, Ouyang H (2019) Lower band gaps of longitudinal wave in a one-dimensional periodic rod by exploiting geometrical nonlinearity. *Mech Syst Signal Process* 124:664–678. <https://doi.org/10.1016/j.ymssp.2019.02.008>
37. Wang K, Zhou J, Cai C et al (2019) Mathematical modeling and analysis of a meta-plate for very low-frequency band gap. *Appl Math Model* 73:581–597. <https://doi.org/10.1016/j.apm.2019.04.033>
38. Lee J, Nomura T, Dede EM (2017) Topology optimization of Halbach magnet arrays using isoparametric projection. *J Magn Magn Mater* 432:140–153. <https://doi.org/10.1016/j.jmmm.2017.01.092>
39. Salauddin M, Park JY (2017) Design and experiment of human hand motion driven electromagnetic energy harvester using dual Halbach magnet array. *Smart Mater Struct* 26:035011
40. Niu S, Liu Y, Wang S et al (2013) Theory of sliding-mode triboelectric nanogenerators. *Adv Mater* 25:6184–6193. <https://doi.org/10.1002/adma.201302808>
41. Cheng S, Wang N, Arnold DP (2007) Modeling of magnetic vibrational energy harvesters using equivalent circuit representations. *J Micromechanics Microengineering* 17:2328–2335. <https://doi.org/10.1088/0960-1317/17/11/021>
42. Wang K, Zhou J, Ouyang H et al (2020) A semi-active metamaterial beam with electromagnetic quasi-zero-stiffness resonators for ultralow-frequency band gap tuning. *Int J Mech Sci* 176:105548. <https://doi.org/10.1016/j.ijmecsci.2020.105548>
43. Wang K, Zhou J, Ouyang H et al (2021) A dual quasi-zero-stiffness sliding-mode triboelectric nanogenerator for harvesting ultralow-low frequency vibration energy. *Mech Syst Signal Process* 151:107368. <https://doi.org/10.1016/j.ymssp.2020.107368>
44. Gatti G, Brennan MJ (2011) On the effects of system parameters on the response of a harmonically excited system consisting of weakly coupled nonlinear and linear oscillators. *J Sound Vib* 330:4538–4550. <https://doi.org/10.1016/j.jsv.2011.04.006>
45. Carrella A, Brennan MJ, Kovacic I, Waters TP (2009) On the force transmissibility of a vibration isolator with quasi-zero-stiffness. *J Sound Vib* 322:707–717. <https://doi.org/10.1016/j.jsv.2008.11.034>
46. Shao JJ, Jiang T, Wang ZL (2020) Theoretical foundations of triboelectric nanogenerators (TEGs). *Sci China Technol Sci* 63:1087–1109. <https://doi.org/10.1007/s11431-020-1604-9>

Publisher's Note Springer Nature remains neutral with regard to jurisdictional claims in published maps and institutional affiliations.